arXiv:1402.1492v1 [astro-ph.CO] 6 Feb 2014

Evidence for particle re-acceleration in the radio relic in the galaxy cluster PLCKG287.0 +32.9

A. Bonafede[1], H. T. Intema[2], M. Brüggen[1],
[1] *Hamburger Sternwarte, Universität Hamburg, Gojenbergsweg 112, 21029, Hamburg, Germany.*
[2] *National Radio Astronomy Observatory, 1003 Lopezville Road, Socorro, NM 87801-0387, USA*

M. Girardi[3,4], M. Nonino[4],
[3] *Dipartimento di Fisica-Sezione di Astronomia, Universitá di Trieste, via Tiepolo 11, I-34143 Trieste, Italy*
[4] *INAF - Osservatorio Astronomico di Trieste, via Tiepolo 11, I-34143 Trieste, Italy*

N. Kantharia[5], R. J. van Weeren[6], H. J. A. Röttgering.[7]
[5] *National center for Radio Astrophysics, TIFR, Post Bag 3, Ganeshkhind, Pune 411 007, India*
[6] *Harvard-Smithsonian Center for Astrophysics, 60 Garden Street, Cambridge, MA 02138, USA*
[7] *Leiden Observatory, Leiden University, 2300 RA Leiden, the Netherlands*

ABSTRACT

Radio relics are diffuse radio sources observed in galaxy clusters, probably produced by shock acceleration during cluster-cluster mergers. Their large size, of the order of 1 Mpc, indicates that the emitting electrons need to be (re)accelerated locally. The usually invoked Diffusive Shock Acceleration models have been challenged by recent observations and theory. We report the discovery of complex radio emission in the Galaxy cluster PLCKG287.0 +32.9, which hosts two relics, a radio halo, and several radio filamentary emission. Optical observations suggest that the cluster is elongated, likely along an intergalactic filament, and displays a significant amount of substructure. The peculiar features of this radio relic are that (i) it appears to be connected to the lobes of a radio galaxy and (ii) the radio spectrum steepens on either side of the radio relic. We discuss the origins of these features in the context of particle re-acceleration.

Subject headings: Galaxy clusters, non-thermal processes

1. Introduction

The hierarchical model of structure formation predicts that clusters of galaxies grow by successive accretion of smaller sub-units. A large amount of energy is dissipated in the intracluster medium (ICM) as a result of merger events, and a fraction of this energy could be channeled into the amplification of the magnetic fields (see e.g. Dolag et al. 2008, for a review) and into the acceleration of high-energy Cosmic Rays (see Petrosian et al. 2008, for a review) that in turn may produce observable extended radio emission. Extended radio sources on a cluster scale, not associated with any optical counterpart, have been detected in a number of galaxy clusters (Venturi et al. 2007; Giovannini et al. 2009; van Weeren et al. 2011; Bonafede et al. 2012; Feretti et al. 2012). They are called radio halos and radio relics, depending on their morphology, location and radio properties.

Radio relics

Radio relics are extended sources, characterised

by a steep spectrum[1] (α >1) and strong polarisation ($\sim$ 20-30 % at 1.4 GHz). Their origin is subject to debate and not yet understood. There is a general consensus that they are related to shock waves, occurring in the ICM during mergers. Shock waves should be able to amplify magnetic fields and accelerate electrons up to relativistic energies, hence producing synchrotron radio emission (Brüggen et al. 2011; Iapichino & Brüggen 2012; Vazza et al. 2012; Skillman et al. 2013). Although this picture is roughly consistent with observations, some important issues remain unexplained. First, a radio relic is not always detected when a shock wave is present in the ICM, as revealed by X-ray observations (Russell et al. 2011) and recently Ogrean et al. (2013) have found a displacement between the X-ray shock wave and the radio relic in 1RXS J0603.3+4214. Secondly, most of the relics do not appear to be co-located with a shock wave in X-ray observations (see review by Brüggen et al. 2011 and ref. therein). Thirdly, shock waves in the ICM are characterised by Mach numbers of the order of 2 - 4 (Skillman et al. 2008; Vazza et al. 2009) so that their efficiency in accelerating particles is expected to be too low to account for the radio emission.
Some authors have proposed that shock waves by themselves are not sufficient to accelerate the particles from the thermal pool to relativistic energies. This would indicate that a seed population of relativistic electrons must be already present before the shock passage (Kang & Ryu 2011; Kang et al. 2012; Pinzke et al. 2013). This seed population of old radio plasma could be reenergised by a shock wave, explaining why the connection between a relic and a shock wave is not one to one. Since the old radio plasma is much more energetic than the thermal gas in the ICM, a low acceleration efficiency could be sufficient to re-accelerate the particles and power the radio emission. The problem is now to find the source for this seed population of relativistic electrons. Some authors have suggested that they come from a previous episode of shock acceleration (Macario et al. 2011). Another possibility is that the old plasma comes from the activity of radio galaxies.

[1]The spectrum is here defined as $S(\nu) \propto \nu^{-\alpha}$.

Recent results by Vazza & Brueggen (2013) have shown that the gamma-ray upper limits to the cluster emission from the *Fermi* satellite are at odds with the hypothesis that radio relics are generated by Diffusive Shock Acceleration (DSA) mechanism, at least in the way it appears to work for supernova remnants. In fact, if shock waves accelerate electrons in the ICM, also protons should be accelerated, with a higher efficiency. In inelastic collisions with the thermal protons, relativistic protons produce pions and gamma-ray photons, which *Fermi* should have detected.

Radio Halos

Radio halos are diffuse Mpc-sized objects found in merging galaxy clusters (e.g. Buote 2001; Cassano et al. 2010) and characterised by steep spectra (see e.g. reviews by Ferrari et al. 2008; Feretti et al. 2012). Two different classes of models have been proposed so far: the hadronic models (Keshet & Loeb 2010; Enßlin et al. 2011) and the turbulent re-acceleration models (Fujita et al. 2003; Cassano & Brunetti 2005). In this paper, we study the peculiar and complex emission of the cluster PLCKG287.0 +32.9 to test DSA models. PLCKG287.0 +32.9 is a massive cluster ($M_{500} \sim 1.4 \times 10^{15}$ solar masses, Planck Collaboration 2013) located at redshift $z = 0.39$, showing a disturbed X-ray morphology (Bagchi et al. 2011) which indicates that the cluster is undergoing a merger event. The X-ray centre of the cluster has a Right Ascension equal to $11h50m51.02s$ and a declination of $-28d04'09.37$" PLCKG287.0 +32.9 is known to host two radio relics (Bagchi et al. 2011). Our new radio observations give a different picture of the system. The radio emission is more complex and more extended than previously observed, and offers a unique opportunity to unravel the origins of radio relics. The paper is organised as follows: In Sec. 2 we present our new observations. The X-ray and optical data are discussed in Sec. 3 and 4, respectively. In Sec. 5 the radio properties are studied, and the spectral properties are presented in Sec. 6. Results are discussed in 7 and we present our conclusions in Sec. 8.
Throughout this paper, we assume a concordance ΛCDM cosmological model, with $H_0 = 71$ km s^{-1} Mpc^{-1}, $\Omega_M = 0.27$, and $\Omega_\Lambda = 0.73$. One arcmin corresponds to 316 kpc at z =0.39.

Table 1: Radio observations.

Frequency MHz	Radio telescope	Observing date	time h	bandwidth MHz	Int. time s	rms noise mJy/beam	Beam
325	GMRT	Jan 2013	7	33	8	0.1	$13'' \times 8''$
610	GMRT	May 2013	10	33	8	0.065	$7'' \times 5''$
150	GMRT	Jul 2011	8	16	8	1.3	$25'' \times 18''$
3000	JVLA	Jun 2013	6	2000	3	0.05	$19'' \times 11''$

Col. 1: Observing Frequency, Col. 2: Radio telescope. Col. 3: Date of the observation. Col. 4: total observing time.

Col. 5: Observing bandwidth. Col 6: Integration time per visibility.

Col 7: 1σ rms noise reached in the high resolution images.

Col 8: FWHM of major and minor axes of the restoring beam in the high resolution images.

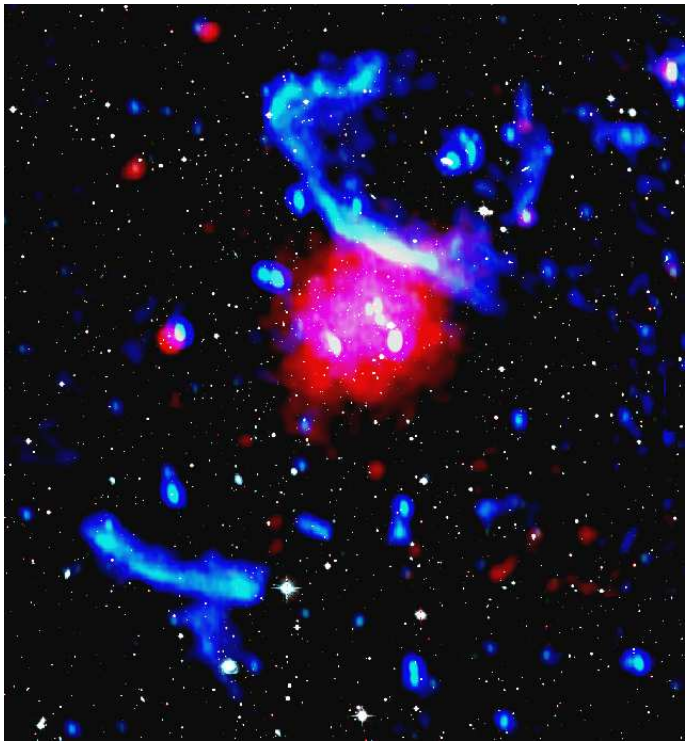

Fig. 1.— X-ray emission in red (XMM-Newton), radio emission at 323 MHz in blue (low resolution, beam FWHM $\sim 22'' \times 18''$) and in green (high resolution: beam FWHM$\sim 13'' \times 8''$).

2. Radio observations

2.1. GMRT observations

The cluster was observed at the Giant Meterwave Radio Telescope (GMRT) at 325 MHz, 610 MHz and 150 MHz (archival data). In Table 1 we list the details of the radio observations. At 323 MHz the observations were recorded using a 33 MHz bandwidth subdivided into 256 channels and 8s integration time. At 610 MHz we used a bandwidth of 33 MHz subdivided in 512 channels and 8s integration time. At 610 MHz the observations were split into two separate observing blocks due to scheduling constraints. We retrieved from the archive observations at 150 MHz. These observations were recorded in one sideband 16 MHz wide, split into 128 channels, and using 8s integration time.

The source 3C147 was observed for 15 minutes at the beginning of the observing block, and used as absolute flux and bandpass calibrator at 150 and 325 MHz, adopting a flux of 64.8 Jy and 53.1 Jy at 150 MHz and 323 MHz, respectively (Scaife & Heald 2012). 3C286 was used as a bandpass and absolute flux calibrator for the 610 MHz observations. Following Scaife & Heald (2012) we adopted a flux of 22.3 Jy. 3C147 was also used to estimate the instrumental contribution to the antenna gains, which is also needed for ionospheric calibration at 323 MHz and 150 MHz (see below). The amplitude and bandpass gains were then directly transferred to the target field. At 150 MHz and 323 MHz the instrumental phase information was also used to correct the target field.

Strong Radio Frequency Interferences (RFI) was removed from the target field data by statisti-

cal outlier flagging tools. Much of the remaining low-level RFI was modelled and subtracted from the data using Obit (Cotton 2008). After RFI removal, datasets have been averaged down to 28 (150 MHz) 24 (323 MHz) and 28 (610 MHz) channels in order to speed up the imaging process and to avoid significant bandwidth smearing.
For the phase calibration, we started from a model derived from the NRAO Vla Sky Survey (NVSS, Condon et al. 1998) and then proceeded with self-calibration loops. We decided not to use a phase calibrator, as the GMRT field of view is wide, and a non-negligible flux is present in the field of the available phase calibrators. We note that using a phase calibrator to bootstrap the flux from 3C147/3C286 would have altered the flux scale, leading to higher errors in the flux measurements. The imaging has been performed using AIPS. In order to compensate for the non-coplanarity of the array we used wide-field imaging technique, decomposing the GMRT field of view into ~ 100 facets. We performed rounds of cleaning and self-calibration, inspecting the residual visibilities for a more accurate removal of low-level RFIs. In order to correct for ionospheric effects, leading to direction-dependent phase errors, we applied SPAM calibration (Intema et al. 2009) and imaging to the target field at 323 and 150 MHz. The presence of strong sources in the field-of-view enabled us to derive directional-dependent gains for each of them (similarly to the peeling technique) and to use these gains to fit a phase-screen over the entire field of view. The final images of the full field-of-view centered on the target were corrected for the primary beam response. We have used the 408 MHz all-sky map by Halsam et at. (1995) to correct for system temperature variations between the calibrator and the target field. The final images are shown in Fig. 3. The highest resolution images are made using the Briggs weighting scheme (robust=-1 in the AIPS definition), and including all the available range of visibilities in the uv-plane (Figs. 2 and 3). As a result, we should be more sensitive to the large-scale emission in the low-frequency bands.
We estimate that the residual amplitude errors are of the order of 6% at 610 and 323 MHz, and $\sim$ 10% at 150 MHz, in line with values reported for GMRT observation at these frequencies (e.g. van Weeren et al. 2009; Intema et al. 2011; Bonafede et al. 2012; Macario et al. 2013).

2.2. VLA observations

Karl G. Jansky Very Large Array (VLA) observations of the cluster were performed in C band (2-4 GHz) in the DnC to C array configuration transition period. Due to scheduling constraints the observations were conducted in three separate scheduling blocks of 2h each. The two base-bands were centered on frequencies of 2.5 GHz and 3.5 GHz. Both have a bandwidth of 1 GHz, covering 2 to 4 GHz continuously. Every baseband is divided into 9 spectral windows, subdivided into 64 channel each, with a frequency resolution of 2 MHz/channel. The integration time was 3s per visibility. This set-up gives a high frequency and time resolution, which is needed to carefully remove the RFIs. However, RFI is severe in the 2-4 GHz band, especially at low elevation. Only 11 spectral windows could be used for imaging and almost 40% of the time has been flagged because of RFIs. The net bandwidth is 1.4 GHz. Details on the observations are listed in Table 1.
Calibration and imaging were performed using the Common Astronomy Software Applications (CASA 4.2). We observed 3C147 as bandpass and absolute flux calibrator, and we used the Perley & Butler (2013) flux scale, which is the most accurate at frequencies above 1 GHz. The source J1146-2447 was observed every $\sim$30 min and it was used as a phase calibrator. We used the multi-frequency multi-scale implementation of the CASA clean to account for the wide bandwidth and the different angular scales of the radio emission. Specifically, we used 2 terms of the Taylor expansion to model the frequency dependence of the sky emission.
We used the peeling technique to derive direction-dependent gains towards a bright source in the field and subtracted it. This bright source has a strongly inverted spectrum ($\alpha \sim -2$) which would complicate the imaging step. Cycles of phase only self-calibration were performed to refine the antenna-phase gain variations on the target field. The residual amplitude errors are estimated to be $\sim$ 6%. The final image was then corrected for the primary beam attenuation, computed for each spectral window separately to account for the wide bandwidth (Fig. 3).

3. X-ray observations

From the XMM-Newton data archive, we have downloaded a 10 ksec observation of the cluster. The X-ray image is shown in Fig. 1. The emission is disturbed and slightly elongated in the NW-SE direction. The X-ray morphology confirms the dynamically perturbed state of the cluster. The Planck collaboration (2011) reports a temperature T_x of 13 keV, and an X-ray luminosity $L_{(0.1-2.4keV)} \sim 1.72 \times 10^{45}\mathrm{ergs}^{-1}$ within r_{500}.

4. Optical analysis

ESO 2.2 m Wide Field Imager (WFI) images[2] were retrieved from the ESO Science Archive. Following the same steps as adopted by Nonino et al. (2009), the images in V-band, R_C-band, and I_C-band were added and reduced to cover about a $30' \times 30'$ field of view. In summary, our stacks were based on a total exposure time of 5400 s in V-band (1.7″seeing), 10 800 s in R_C-band (1.0″), and 6000 s in I_C-band (0.8″). The astrometric solutions were obtained using 2MASS as reference. Unfortunately, the observations in all filters were collected under non-photometric conditions, as shown from the relative photometric analysis. Therefore, the final stacked images were not calibrated with standard stars. For the color selection, we used 2MASS to make a first-order calibration. The absolute zero-point calibration was estimated to be accurate to within 0.2 mag. We obtained a photometric catalog of $\sim$ 50 000 objects using SExtractor

[2]Based on observations made with ESO Telescopes at the La Silla Paranal Observatory under programme ID 086.A-9028(B).

Table 2: 2D substructure from the WFI photometric sample.

Subclump	N_S	α(J2000), δ(J2000) h : m : s, ° : ′ : ″	ρ_S	χ^2_S
NWc	101	11 50 49.2 − 28 04 58	1.00	68
SEc	230	11 50 52.4 − 28 05 30	0.92	78
NW	92	11 50 44.9 − 28 03 23	0.52	46
SEext	91	11 51 03.5 − 28 11 56	0.20	26

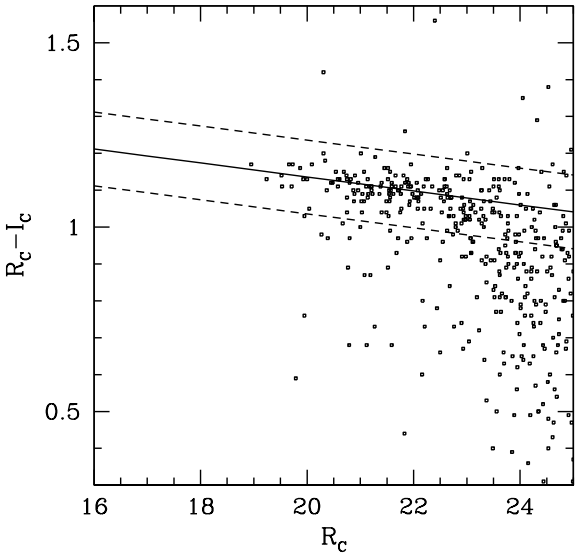

Fig. 4.— WFI R_C–I vs. R_C diagram for galaxies within the 0.5 Mpc cluster region available. The solid line gives the CMR obtained from the fit and the dashed lines are drawn at ±0.1 mag to indicate the region used to define the likely member galaxies in the entire photometric catalog.

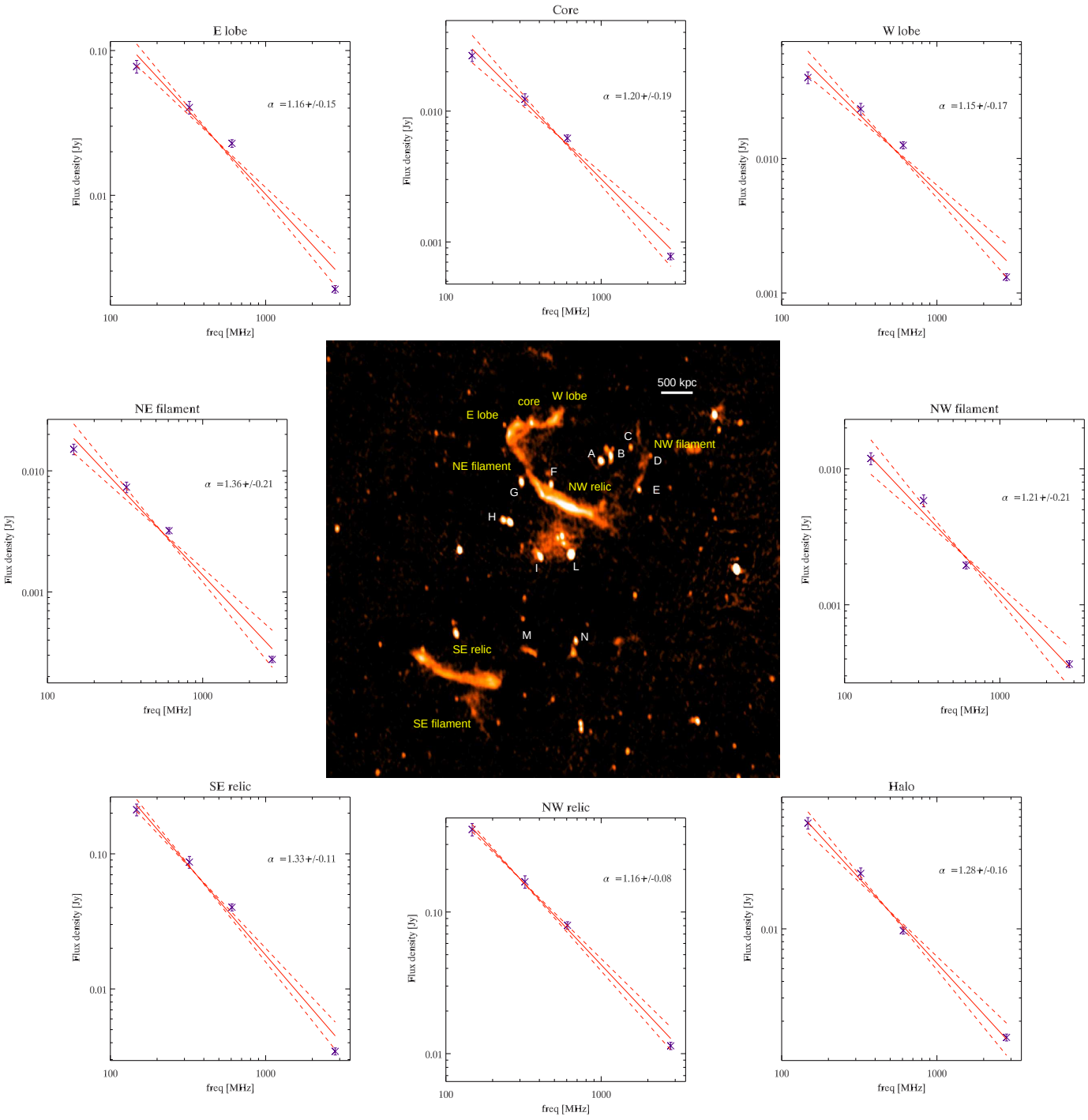

Fig. 2.— Central panel: Radio emission at 323 MHz. Yellow labels indicate the diffuse sources detected in the cluster field. White labels mark the embedded radio-galaxies. The surrounding panels show the spectral index fits for the extended emission in the cluster. The continuous line shows the attempt to fit a power-law from 150 MHz to 3 GHz, the dashed lines are the fit 1σ errors. Note that the flux has been measured only where the emission is detected above 3σ at all frequencies.

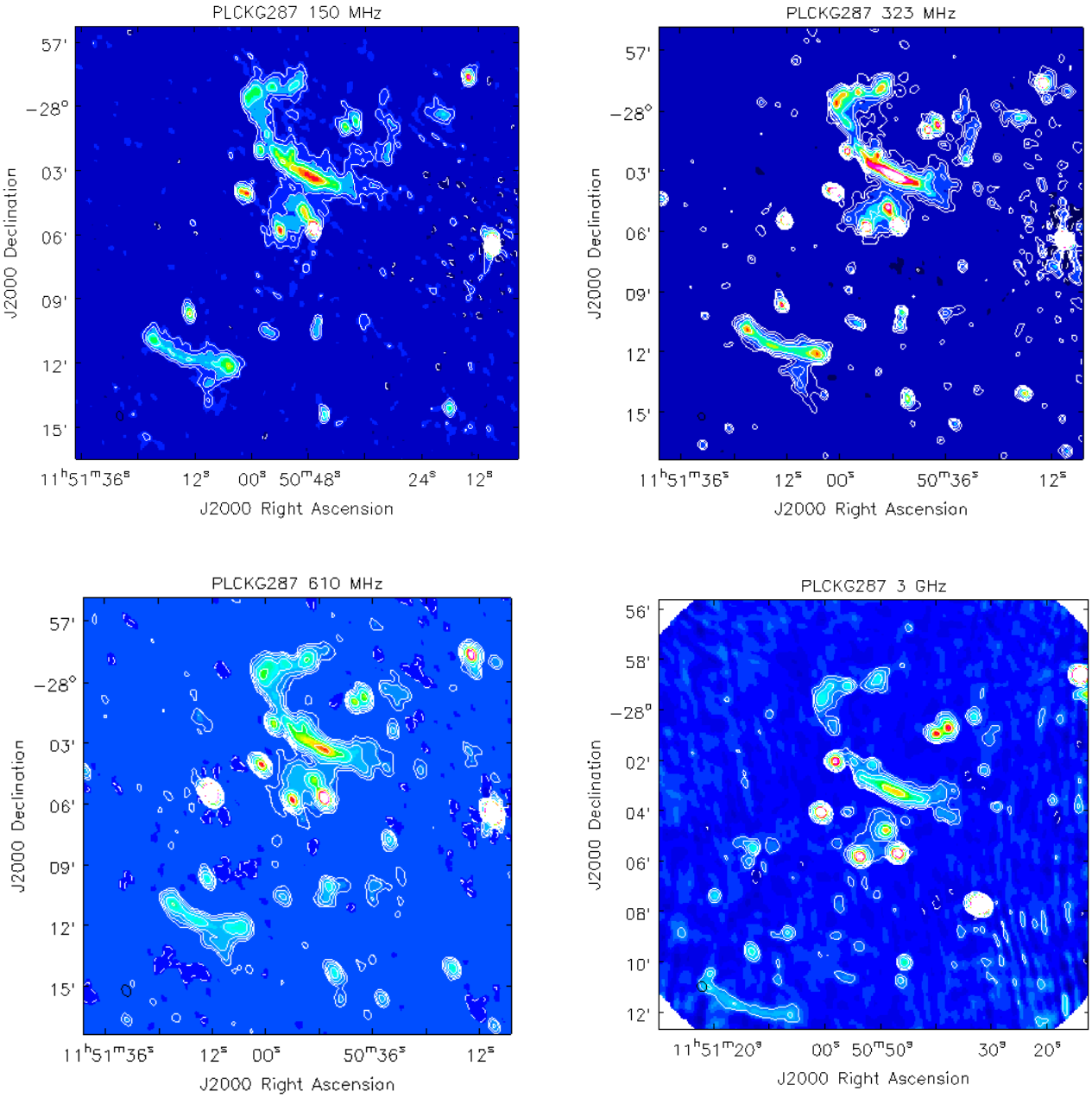

Fig. 3.— Radio emission from PLCKG287.0 +32.9 at 150 MHz (top, left), 323 MHz (top, right), 610 MHz (bottom left), and 3 GHz (bottom right.) The image at 150 is obtained with a Briggs weighting scheme, intermediate between uniform and natural weighting, to lower the side-lobes of the primary beam. The image at 323 MHz is obtained using a Gaussian taper to enhance the diffuse emission. The images at 610 MHz and 3 GHz are obtained cutting the longer baselines and using a Gaussian taper. Contours start at $\pm 3\sigma$ and are spaced by a factor 2. The 1σ values are are 1.3 mJy/beam (150 MHz), 0.15 mJy/beam (323 MHz), 0.13 mJy/beam (610 MHz), and 30 μJy/beam (3 GHz).

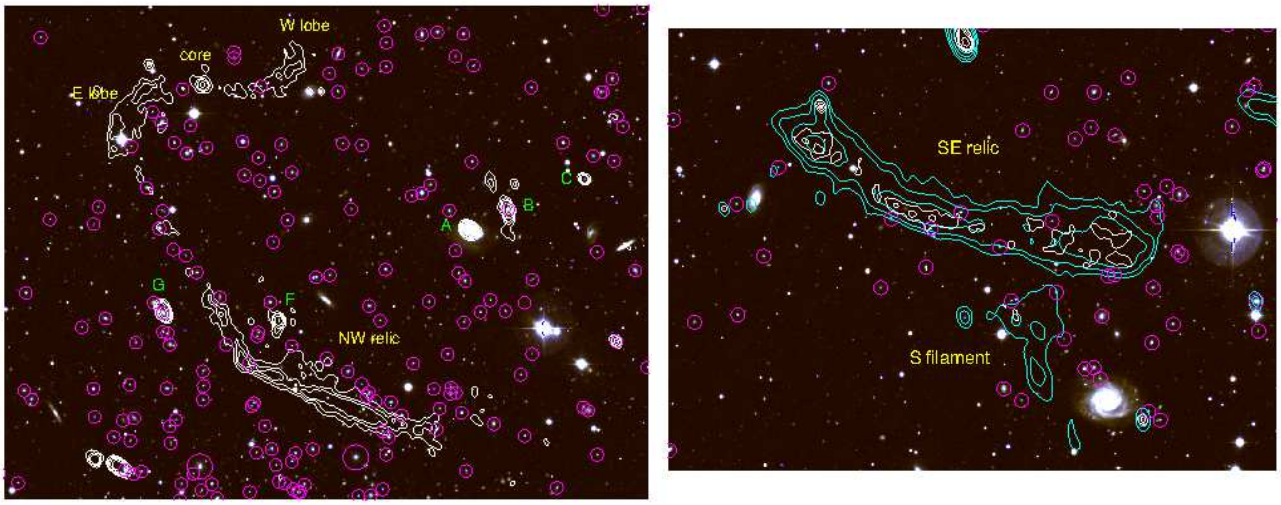

Fig. 5.— The NW (left) and SE relic (right): optical emission in colours. Magenta circles indicate the likely members with $R < 22$, white contours are from 610 MHz high-resolution observations. The beam is $\sim 7'' \times 5''$, contours start at 3σ (0.195 mJy/beam) and are spaced by a factor 2. In order to highlight the SE relic, 323 MHz contours are plotted in cyan. The beam is $\sim 13'' \times 8''$, contours start at 3σ (0.3 mJy/beam) and are spaced by a factor 2. Labels indicate the radio sources (as in Figure 2.)

(Bertin & Arnouts 1996).

After a preliminary rejection of stellar objects using the flux radius Sextractor parameter, we selected likely members on the basis of the (R_C–I vs. R_C) color-magnitude relation (hereafter CMR). Due to the limitations in the V-band data, we preferred to not use them to improve the member selection. In order to determine the CMR, we applied the 2σ-clipping fitting procedure to the galaxies within 0.5 Mpc of the cluster center. For the center of PLCK287+32.9, we adopted the position of the BCG [R.A.=$11^h50^m50^s.1$, Dec.=$-28°04'55.3''$ (J2000.0)]. The resulting CMR is R_C–I=1.52($\pm$0.07) − 0.019($\pm$0.03)× R_C (see Fig. 4). Out of our photometric catalog, we considered *likely* cluster members to be those objects lying within 0.1 of the CMR. Density reconstruction of the 2D galaxy distribution was performed through the 2D-DEDICA adaptive kernel method (Pisani 1993). The cluster structure is elongated along the NW-SE direction and exhibits significant substructure both in central and external regions (R_{500}[3] ∼ 1.6 Mpc; Planck Collaboration, 2011). In particular, Figure 6 shows the contour map for the likely cluster members having $R_C \leq 22.5$, thus sampling the galaxy luminosity function down to ∼ 1.5 mag fainter than R_C^* (1473/633 galaxies in the whole field/R_{200}-region). Table 2 lists information for the four most significant (>> 99% confidence level) density peaks: the number of assigned members, N_S (Col. 2); the peak position (Col. 3); the density (relative to the densest peak), ρ_S (Col. 4); the value of χ^2 for each peak, χ^2_S (Col. 5). These main features are quite robust with respect to changes in the magnitude limit. In the very central region the main feature is the presence of two comparable very dense peaks at NW and SE (hereafter NWc and SEc), the former coinciding with the BCG. In the external region, the main feature is the presence of a SE peak (hereafter SEext) at ∼ R_{200}. The corresponding SEext group is clearly a minor substructure comprising ∼ 20% (∼ 15%) of galaxies contained within R_{500} (R_{200}).[4] As for the direction of the cluster elongation, the position

[3]The radius R_δ is the radius of a sphere with mass overdensity δ times the critical density at the redshift of the galaxy system.

[4]See also its low density with respect to the two main peaks SEc and NWc as listed in Table 2.

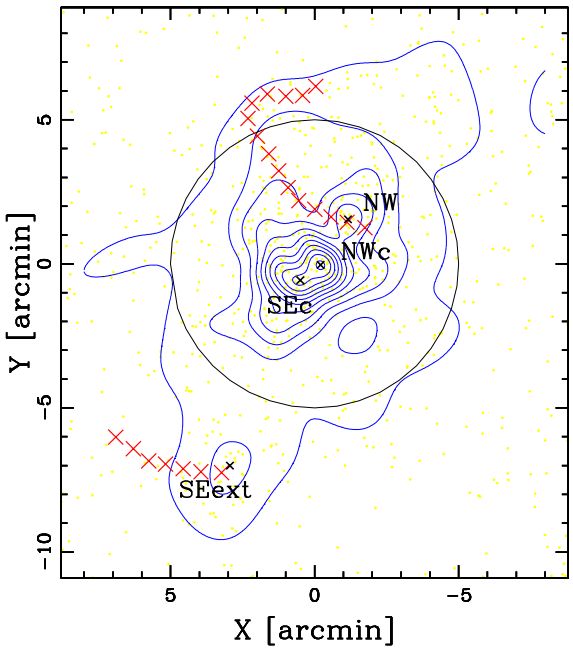

Fig. 6.— Spatial distribution on the sky and relative isodensity contour map of the photometric likely cluster members with $R_C \leq 22.5$, obtained with the 2D-DEDICA method. The BCG position is taken as the cluster center. The circle indicates the $5'$ region, i.e. $\sim$ 1.6 Mpc at the cluster redshift, and corresponding to $\sim R_{500}$. Large red crosses indicate, in a schematic way, the southern and northern relic features. Small black crosses and labels indicate the density peaks listed in Table 2.

angle of the galaxy distribution (here measured counter–clock–wise from north) becomes larger when considering a more extended cluster region out to $\sim R_{500}$: from PA $\sim$ 120 degrees at $0.5R_{500}$ to PA $\sim$ 160 degrees at $\sim R_{500}$.

5. Cluster radio emission

In this section we describe the different radio emitting parts of the cluster PLCKG287.0 +32.9. Two radio relics and hints of radio halo emission are visible in the NVSS and TGSS (Bagchi et al. 2011). Our observations reveal that the N relic discovered by Bagchi et al. (2011) is actually a radio galaxy, and that another relic is present closer to the cluster center. A radio halo is definitely established, and additional filamentary emission is detected around the relics. The wide frequency range covered by our observations allows us to perform a spectral analysis and investigate the origin of the observed emission.

5.1. The northern relic and the filamentary structure

The cluster is imaged with a sensitivity that is 5-7 times better than the reprocessed TGSS observations analysed by Bagchi et al. (2011), and a resolution that is ∼4-8 better than TGSS and NVSS, allowing us to detect additional diffuse emission and to analyse the morphology and spectral properties of the different components. Our observations provide a different view of the radio emission compared to the one given by Bagchi et al. (2011). The source called northern relic (RN) in Bagchi et al. (2011) is actually a radio galaxy, composed of two lobes that are edge-brightened. The emission of the E lobe is connected to the NW relic (which is called Y-shaped filamentary radio feature in Bagchi et al. 2011). The NW relic dists in projection $\sim$ 350 kpc from the cluster X-ray centre.

We detect a low-brightness filamentary structure that departs from the NE tip of the relic and bends towards the W, increasing its brightness, towards a structure that looks like a radio galaxy with a core and two bent lobes (core, E lobe and W lobe in Fig. 2). This emission is not detected at 3 GHz, where the candidate radio galaxy and the relic are disconnected. This indicates that the

Table 3: Properties of the cluster radio sources.

Source name	Frequency MHz	Flux density mJy	LAS "	LLS kpc
NW relic	150	620	494	2598
	323	216	420	2209
	610	110	440	2314
	3000	15.2	360	1894
NE filament	150	52	70	368
	323	18	70	368
	610	7.6	70	368
	3000	0.62	60	316
NW filament	150	84*	240	1262
	323	14.5	235	1236
	610	5.4	130	684
	3000	0.43**	80	421
lobeW	150	75	95	500
	323	33	100	526
	610	33	138	725
	3000	1.7	120	631
lobeE	150	95	100	526
	323	45	100	526
	610	31	100	526
	3000	2.7	80	421
core	150	30	-	-
	325	13.9	-	-
	610	3.9	-	-
	3000	0.65	-	-
Halo	150	314	450	2104
	323	63	250	1315
	610	26	250	1315
	3000	2.9	180	946
SE relic	150	382	321	1689
	323	114	315	1660
	610	50	305	1604
	3000	5.2	280	1472
Sfilament	150	61*	120	631
	323	17	160	841
	610	6.5	120	631
	3000	-	-	-
Total north emission	150 MHz	1110	630	3314
N filament	150	33	270	1420

Col. 1: Source name, Col. 2: Observing frequency, Col. 3: Flux density integrated above 3σ from the low-resolution maps and subtracting the emission of the embedded radio galaxies. Col. 4: Largest angular scale of the emission; Col 5: Largest linear scale.

* At low resolution the emission blends into the one of the nearby source, and cannot be unambiguously separated.

** Only bright spots are detected

Table 4: Flux density of the radio-galaxies.

Freq. MHz	A mJy	B mJy	C mJy	D mJy	E mJy	F mJy	G mJy	H mJy	I mJy	L mJy	M mJy	N mJy
150	24	16	3	-	9	15	25	69	44	193	17	21
323	16.0	13.2	2.7	1.2	4.4	8.6	14.9	32	28	94	6.3	10.9
610	10.4	9.3	2.0	1.1	2.4	6.5	10.5	19	20	55	3.7	10.2
3000	2.7	3.4	0.66	-	0.22	0.65	1.03	5.2	4.6	6.8	-	-

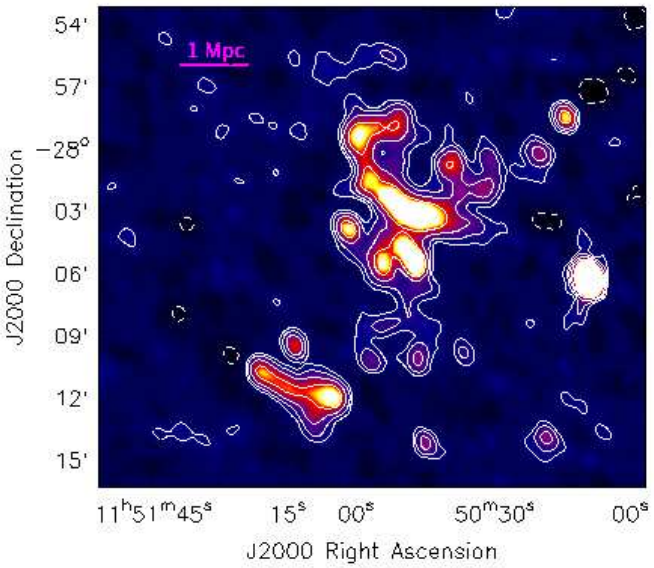

Fig. 7.— Radio emission at 150 MHz in colours. The image is obtained tapering down the baselines longer than 5 kλ to enhance the diffuse emission. The beam is $\sim$ 50" $\times$ 40", the rms noise is $\sim$2 mJy/beam. Contours are drawn at $\pm 3\sigma$ and are spaced by a factor 2.

electrons producing the relic region come from the radio galaxy (see Sec. 7). However, no optical counterpart to the core has been found (Fig. 5). We discuss this scenario in Sec. 7.

At its SW tip, the relic emission becomes less elongated and more roundish. The brightness profile of the relic is symmetric with respect to the major axis of the relic, with its maximum in the central part. Towards the cluster center, the emission merges into the radio halo. In the 3 GHz image, this connection between the radio halo and the relic is not detected. A radio bridge connecting a radio halo with a relic has been observed in other clusters (e.g. Coma, Giovannini et al. 1993).

Another radio filament is detected at 150 and 323 MHz close to the SW tip of the NW relic and elongated perpendicular to the relic's major axis (NW filament). At 150 MHz, this filament is attached to the SW part of the relic, while at 323 MHz it is detached. At 610 MHz and 3 GHz only a small bright spot of the filament is detected. However, due to the different coverage of the short uv-spacing, it is not possible to draw firm conclusions on the spectrum of this region (see discussion about spectral index in Sec. 6). In order to highlight, the full extent of the radio emission, we have imaged the datasets while tapering down the long baselines (Figs. 3 and 7). At 323 MHz and 150 MHz, more diffuse emission is detected beyond the relic, towards the cluster outskirts. At 150 MHz, this emission encompasses all the different structures detected at higher resolution. The total extent of the northern emission, considered as a whole, is $\sim 10'$, corresponding to a linear scale of $\sim$ 3.3 Mpc at the cluster's redshift. Such a large extension is not detected in the other bands because of the reduced sensitivity to the large angular size compared to the 150 MHz observations, combined with the spectral properties of the emission. Another filamentary source, 1 Mpc wide, is detected at 150

MHz north of the radio-galaxy (see Fig. 7).
Flux densities, dimensions and other properties of the radio emission around the NW relic are listed in Table 4 and labelled in Fig. 2. The flux of the extended components has been measured from the low-resolution images after subtracting the contribution of the embedded sources (Table 4). However, at 150 MHz the different components are merged into a single patch of emission, and there is no unique way to define the borders of the relic, filaments and lobes. Hence, we also measure the total flux of the emission in the NW (relic, filaments, lobes and additional diffuse emission detected NW of the relic).

5.2. The radio halo and the southern tail

Our observations confirm the presence of a radio halo, as suggested by Bagchi et al. (2011). The halo emission merges into the northern relic and has a roundish shape. At 323 MHz, the radio halo emission roughly follows the X-ray emission of the cluster, as found in other cases (see review by Feretti et al. 2012). At 150 MHz, the low-resolution image reveals a southern extension of the radio halo (Fig. 7). This southern component has no counterpart in the X-ray image of the cluster, has a lower surface brightness with respect to the radio halo, and a "double tail" shape, merging into two radio galaxies. The total extent of the radio emission is about $450''$, corresponding to 2.3 Mpc at the cluster redshift. Excluding the southern component, the roundish halo has a total extent of $\sim 250''$ (1.3 Mpc). Further details are listed in Table 4.

5.3. The southern radio relic and the southern filament

A second relic is located at a projected distance of 2.8 Mpc from the X-ray center, south of the subgroup detected through the optical analysis (Sec. 4). The SE relic is elongated in the direction NE-SW parallel to the NW relic and perpendicular to the mass distribution as traced by the galaxies (see Fig. 6). It has a classical "arc-like" morphology detected in other relics (e.g Rottgering et al. 1997; Bagchi et al. 2006; van Weeren et al. 2010). As noted by Bagchi et al. (2011) the SE relic appears (in projection) much farther from the cluster center, as detected from X-ray emission, than the NW relic. Optical data reveals a group of galaxies south of the main cluster. This southern clump is likely a sub cluster, not visible in the X-ray image, which is interacting with the main cluster. This situation could be similar to the one observed in the Coma cluster, where a relic is located behind a sub-group interacting with the main cluster. Alternatively, the galaxies in the southern clump could be in the process of accreting towards the main cluster through a cosmic filament with little hot gas.
New emission is detected in the region of the SE relic (SE filament in Fig. 2). It has a filamentary morphology and it is elongated almost perpendicular to the SE relic major axis, with a maximum extension of ~ 850 kpc towards south at 323 MHz. The relic is barely visible in the 3 GHz image because of the primary beam attenuation. Contrary to the radio halo and to the NW emission, no further emission is detected ahead of the SE relic in the lower frequency images.

6. Spectral index study

In this Section, we analyse the spectral index maps based on the combined GMRT and JVLA observations as well as on the GMRT maps only. The latter is relevant to study the spectral properties of the emission that is not detected at high frequency (3 GHz).

Using the high-resolution images, we have checked for possible systematic positional offsets in different datasets. These offsets can be generated in the process of self-calibration or ionospheric-phase corrections. Sources detected in the 323 MHz map with a signal-to-noise ratio > 10 have been used to calculate the offsets relative to the NVSS (83 sources were found). We have repeated the same procedure for the other images, taking now as a reference the shifted 323 MHz map. We have found 85 sources, 130 sources and 18 sources in the 150 MHz, 610 MHz and 3 GHz map, respectively. The resulting offsets are small (less than $1''$), and smaller than the grid resolution used to image the datasets ($4''$). Nonetheless, we have corrected for them by shifting the visibilities before Fourier-transforming them into the imaging plane. The datasets have been imaged using the same range of baselines in the uv-plane (0.35 - 12.5 kλ), gridding the data onto the same grid,

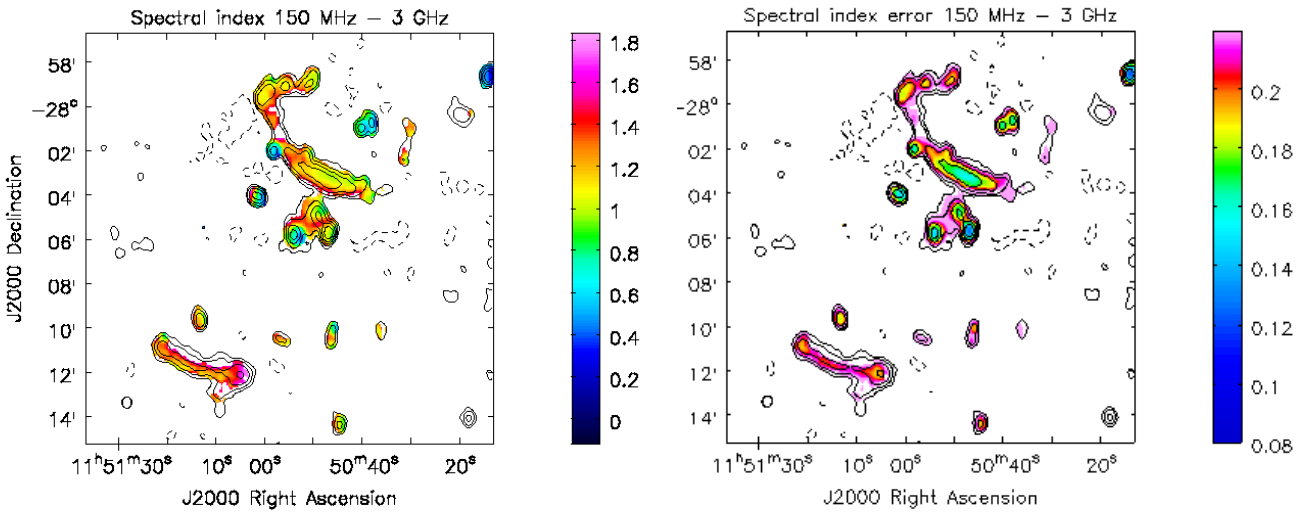

Fig. 8.— Spectral index and spectral index error image obtained considering 150, 323, 610, and 3000 MHz images (colours). 150 MHz contours are overlaid. Note that much of the extended emission is not shown because of the common uv-range used, required to minimise instrumental effects.

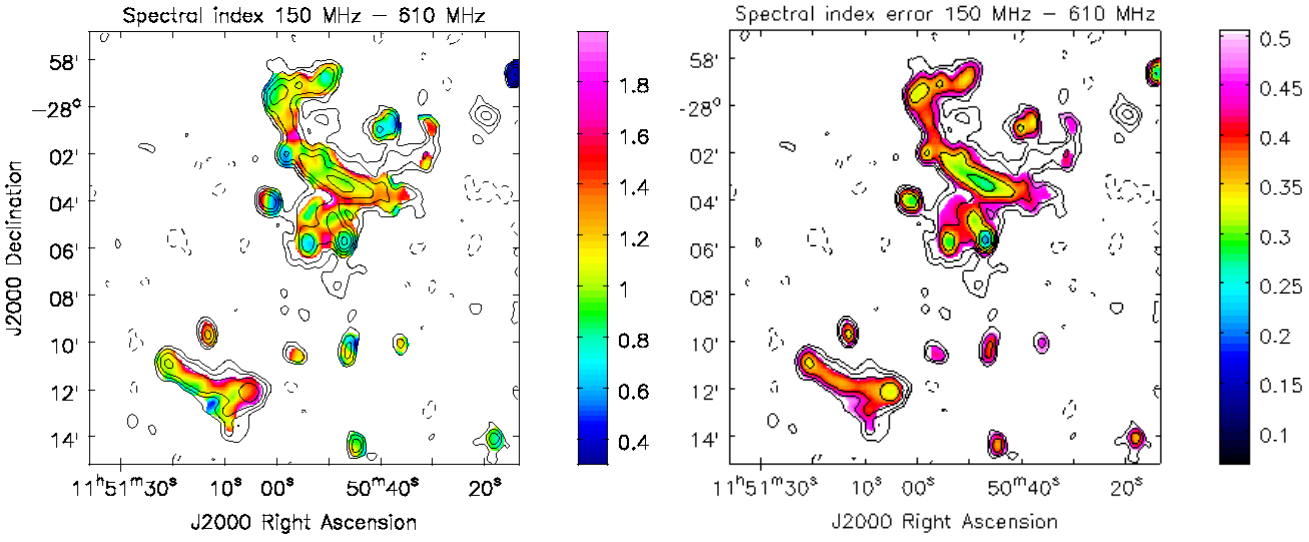

Fig. 9.— Spectral index and spectral index error image obtained considering 150 323 and 610 MHz images (colours). 150 MHz contours are overlaid.

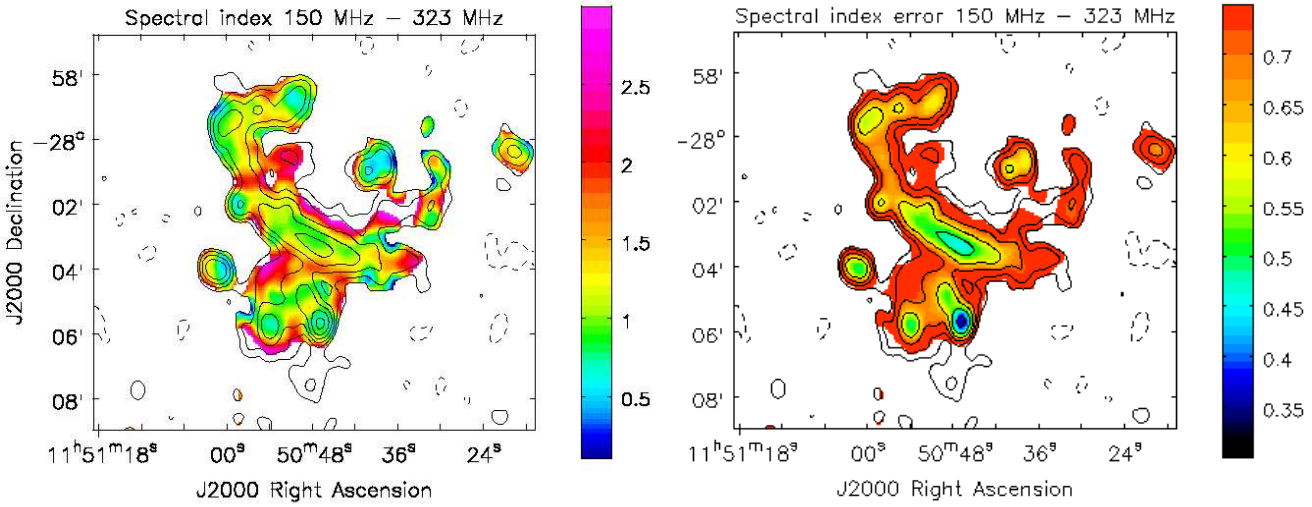

Fig. 10.— Spectral index and spectral index error image obtained considering 150 and 323 MHz images (colours). 150 MHz contours are overlaid.

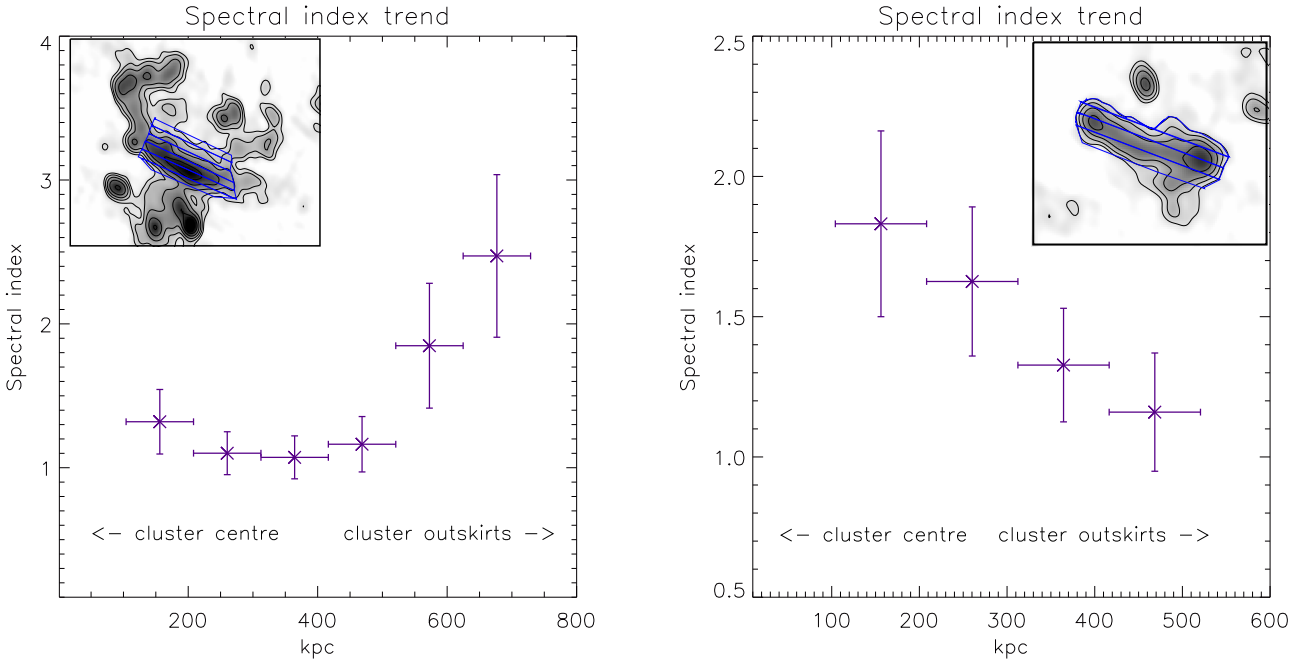

Fig. 11.— Spectral index in the NW (left panel) and SE relic (right panel). The spectral index is computed in the boxes shown in the panels. The spectral index has been computed between 150 and 610 MHz.

and tapering the long baselines (using a circular Gaussian taper of 8 kλ) to enhance the diffuse emission.

After cleaning, each image has been corrected for the primary beam response and convolved with the same Gaussian beam (FWHM of the beam $30'' \times 28''$). We have then fitted the spectrum using a linear model minimising the chi-square error statistics wherever the emission was detected above 3σ at all frequencies. We note that this introduces a bias towards the flattest spectral index regions, that can be detected up to 3 GHz.
The spectral index image is displayed in Fig. 8. Since the FWHM of the convolution beam is sampled by ~ 64 pixels in the images, while the fit has been performed pixel by pixel, this image is only meant to show the general features of the spectral index distribution. In addition, the uv-plane distributions remain quite different, even after the uv restrictions that we have applied. Hence, the spectral index maps have to be treated with caution. In order to improve the significance of the spectral index variation across the relic, we have integrated the flux over larger regions (see Sec. 6.1, 6.2, 6.3, and Fig. 2). Embedded sources have been masked.
The VLA and GMRT observations have a very different coverage of the uv-plane. Additional differences come from the different observing time and different sensitivities. For these reasons, it is not possible to derive a spectral index distribution for the weak diffuse components detected in this cluster using all the observations.
We have derived the spectral index distribution at low frequencies by considering the GMRT observations only, to study the spectral properties of the emission not detected at high frequency (we imaged the common uv-range 0.12 - 12.5 kλ and used a circular taper as above). The spectral index image, shown in Fig. 9, shows more of the diffuse emission. We have overlaid the 150 MHz contours from which the spectral index map is derived to point out that even excluding the 3 GHz image, the spectral index could be derived only in certain parts of the image. At 150 MHz, additional emission is detected especially around the NW relic and the radio halo. This emission is less extended at 323 MHz and not visible at 610 MHz above 3σ. Since we have selected the visibilities in the same uv-range, we can conclude that the synchrotron emission is steep ($\alpha > 2$) and hence harder to detect at higher frequencies (see however 6.4 for possible artefacts on the spectral index.).

6.1. The NW relic and northern emission

The spectral index distribution in this region shows a gradient along the relic's minor axis, a steepening in the NE filament, and a flattening again towards the lobes of the radio galaxy. The integrated spectral index in the NW relic is shown in Fig. 2, and is well-represented by a single power law from 150 MHz up to 3 GHz. In order to recover as much information as possible for the extended emission detected NW of the NW relic, we have created an additional spectral index map using only the 150 MHz and 323 MHz observations (Fig. 10). Some important trends are visible in the relic. The spectral index shows a gradient along the relic minor axis, with the flattest part located towards the diffuse emission detected NW of the relic. The spectrum steepens gradually towards the cluster center, and more sharply towards the NW diffuse emission in the cluster outskirts up to $\alpha \sim 3.1$. To show this gradient more clearly, we have integrated the flux in the regions displayed in Fig. 11, and fitted the spectral index in each region separately. Considering only the regions where the flux density is above 3σ in all the maps would introduce a bias towards low spectral indexes since the emission becomes wider towards lower frequencies. To remove this bias, we have integrated the flux density at 150, 323 and 610 MHz in shells parallel to the relic major axis, considering all the pixels where the emission at 150 MHz is above 3σ. We have fitted the spectral index in each shell, taking into account only the flux densities where the flux was above 3 times the error, estimated as $\sigma \times \sqrt{n_{beam}}$ (see e.g. Orrú et al. 2007; Bonafede et al. 2009). In the two outer shells, the flux density at 610 MHz is below this limit, hence only an upper limit can be derived. We have checked that the upper limits are consistent with the spectral index obtained using 150 MHz and 323 MHz flux densities. In Fig. 11 the spectral index in the shells is displayed. The flattest part is in the central shell, located at the edge of the relic emission, with an average value of $\alpha = 1.07 \pm 0.17$. Towards the cluster center, the spectral index steepens gradually with $\alpha = 1.10 \pm 0.17$ and $\alpha = 1.31 \pm 0.26$

Table 5: Integrated spectral index in the various regions.

	W Lobe	Core	E Lobe	NW relic
α	1.15 ± 0.17	1.20 ± 0.19	1.16 ± 0.15	1.36 ± 0.21

	NE filament	Halo	SE relic	NW filament
α	1.16 ± 0.08	1.28 ± 0.16	1.33 ± 0.11	1.21 ± 0.21

in the inner shell close to the halo emission. Towards the outskirts of the cluster - where diffuse emission is detected only at the lower frequencies - the spectral index steepens with values of $\alpha = 1.15 \pm 0.23$, $\alpha = 1.85 \pm 0.55$, and $\alpha = 2.47 \pm 0.60$. If we assume that the particles are being accelerated by a shock that is moving outwards, in the shell that displays the flattest spectral index the corresponding Mach number M would be $M \sim 5.4$, assuming stationarity and continuous injection. In this case, the trend towards the cluster center can be explained with synchrotron ageing, but the steep emission detected ahead of the relic is more difficult to explain (see Sec. 7). It is worth mentioning that recent simulations of one galaxy cluster (Skillman et al. 2013) are able to reproduce small spectral index variations across radio relics without considering radiative losses. They show that the complex shock structure and projection effects are in principle able to reproduce spectral index trends. Hence, the steepening in an unexpected direction, NW of the NW relic in our case, does not necessarily imply ageing. At the same time, the steepening that we attribute to ageing could be contaminated by projection effects. The Mach number we derive from the NW relic spectral index would be rare for merger shock waves, although not impossible (e.g. Skillman et al. 2008; Vazza et al. 2011). However, radio-derived Mach numbers are notoriously unreliable (e.g. Skillman et al. 2008). The spectral index steepens towards the NE filament, becomes flatter in the E lobe, steepens again towards the core and flattens again in the W lobe. The spectral index value in the core is around $\alpha \sim 1$, hence steeper than the one typically detected in the core of radio galaxies. The trend in the lobes and the flat value of the spectral index detected at the edge of the lobes is typical of FR type II radio galaxies. In Fig. 2 we show the attempts to fit the emission in the lobes, in the core, in the NE and NW filament with a single power-law (see also Table 5). The spectral index in these regions seem to deviate from a single power law. In the NE filament the spectrum is curved, as well as in the lobes and in the core. The spectral index in the NW filament, instead, shows a steepening at frequencies > 323 MHz and flattens between 610 MHz and 3 GHz. The curved spectra detected in the lobes, core and in the NE filament suggests that the core is not a core of the candidate radio-galaxy, but rather a distant radio source, and that the plasma emitting in the NE filament was old radio plasma which has undergone adiabatic compression, pushing the synchrotron cut-off to higher frequencies. The optical counterpart could be the small galaxy observed E of the core, although it is likely not a massive elliptical as one would expect. The fact that no jet emission is visible indicates that the radio-galaxy is no more active now, hence a rather faint radio core is not surprising.

The spectral index trends detected in these regions suggest that we are witnessing the process of shock re-acceleration. The old plasma is supplied by the lobes of a radio-galaxy whose nucleus is turned off, and possibly a shock wave is compressing the plasma in the NE filaments and accelerating the particles in the relic. We will discuss this possibility in more detail in Sec. 7.

6.2. The radio halo

As for the emission around the NW relic, the measured extent of the radio halo becomes smaller going from 150 MHz to 3 GHz. The southern extension is detected only at 150 MHz, indicating that the spectral index must be steeper than $\alpha = 3$ in that region. The spectral index distribution across the radio halo is quite patchy and no clear trend can be detected. If we restrict our analysis to the GMRT observations, the halo is better imaged. In the spectral index maps be-

tween 150 MHz and 610 MHz and between 150 MHz and 323 MHz some interesting features are detected. A patch with a flat spectral index is located in the NE part of the halo ($\alpha^{610\rm MHz}_{150\rm MHz} \sim 0.8$) which shows a steep spectrum between 150 MHz and 323 MHz ($\alpha^{323\rm MHz}_{150\rm MHz} \sim 2.6$). This difference is significant although the errors in the spectral index map are large. We have computed the spectrum in this region separately, deriving an average spectral index of $\alpha^{323\rm MHz}_{150\rm MHz} = 1.7 \pm 0.6$ and $\alpha^{610\rm MHz}_{332\rm MHz} = 0.3 \pm 0.6$, which within 1σ error are incompatible with a power law. The non-detection at 3 GHz is suggesting that the spectrum steepens again above 610 MHz, but due to the missing short baselines no firm conclusions can be drawn. A similar behaviour has been observed in the radio halo of Abell 2256 (van Weeren et al. 2012), where a steepening of the spectrum in one small region of the halo has been interpreted as due to a mixed population of primary and secondary particles, or as an indication of particle re-acceleration by inhomogeneous turbulence. We have fitted the spectral index between 150 MHz and 3 GHz (Fig. 2), restricting to the area of the halo detected at all frequencies. Within the errors, the integrated spectrum is compatible with a single power law.

Estimating the power of the radio halo at 1.4 GHz is not easy. The size of the halo more than doubles between 150 MHz and 3 GHz. Since most of the radio halos used to compute the correlation have been observed either at 1.4 GHz or at 300 MHz or 610 MHz, we have extrapolated the flux from the 610 MHz measurement assuming a spectral index of 1.28. The corresponding power of the radio halo at 1.4 GHz, including the K-correction, would be $5.1 \times 10^{24}\,\rm WHz^{-1}$ at 1.4 GHz, which is a factor ~ 4 lower than what expected from the $P_{1.4GHz} - L_x$ correlation (e.g. Cassano et al. 2013) and $P_{1.4GHz} - SZ$ correlation (Sommer & Basu 2013). If we extrapolate the flux from 150 MHz, including the Southern tails of radio halo and assuming a straight spectral index of 1.28, we would obtain a total flux of 17.5 mJy at 1.4 GHz, corresponding to a radio power of $1.0 \times 10^{25}\,\rm W\,Hz^{-1}$, which is only a factor 2 below the $P_{1.4GHz} - L_x$ and consistent with the $P_{1.4GHz} - SZ$ correlation. This value should be taken as an upper limit to the power at 1.4 GHz, since the spectral index could be steeper than 1.28 in the regions detected only at 150 MHz.

6.3. The SE relic

The SE relic spectral index shows a steepening towards the cluster center, as expected from DSA models and detected in other cases (e.g. Bonafede et al. 2009; van Weeren et al. 2010; Giacintucci et al. 2011; Bonafede et al. 2012). The resolution obtained after the uv-range cut is not sufficient to properly distinguish the SE radio filament from the relic emission. The emission from 150 MHz to 3 GHz can be represented by a single power-law (Fig. 2), and the average spectral index is steep ($\alpha = 1.33 \pm 0.11$).
As for the halo and the emission SE of the SE relic, more diffuse emission is detected at 150 MHz and at 323 MHz. We have computed the spectral index in shells parallel to the relic major axis, wherever the 150 MHz emission is above 3 σ, as we have done for the NW relic. The spectral index profile is shown in Fig. 11. The first shell, closer to the cluster center, exhibits the steepest spectrum, $\alpha = 1.83 \pm 0.33$ which is computed using only 150 MHz and 323 MHz images, as the emission at 610 MHz falls below 3σ. We have checked that the upper limit derived from the 610 MHz observation is consistent with the derived value of α. The spectral index flattens towards the outskirts of the cluster, up to a value of $\alpha = 1.16 \pm 0.22$. If we use this value to derive the Mach number of the shock wave responsible for the radio emission (i.e. if we assume that particles are accelerated in this region), we obtain $M \sim 3.7$ under the assumptions of stationarity and continuous injection.

6.4. Imaging artefacts and warnings on spectral index studies

Although the efforts in minimising the instrumental differences among the observations, interferometric imaging can lead to artefacts in spectral index studies, especially at the edge of extended emissions. The three sources of artefacts are:
(i) Uneven sampling of the short baselines in different observations. Spectral index maps tend to artificially steepen at the edge of extended emission regions mainly because of under-representation of the extended emission at higher frequencies. Restricting the imaging to the common range of sampled visibilities in the uv-plane reduces this problem. However, differences in the uv-plane sampling still remain, also in those parts that are

sampled by all datasets.
(ii) Noise-induced flux boosting in the higher-frequency maps. Spectral index maps can show a flattening at the edge of extended emission regions due to noise-induced flux boosting in the higher-frequency maps.
(iii) Imaging artefacts. Spectral index maps generated from individual intensity maps at several frequencies are much more sensitive to the way the imaging is done than the intensity maps themselves. This is because the spectral index is determined by taking the ratio of maps at different frequencies, which tends to magnify any small variation that was present but hard to recognise in the intensity maps. Such magnified variations will create a patchy spectral index map, which may be what we see in the NW relic region in the spectral index maps (Figs. 8, 9, and 10).
Systematic errors like these do not cancel out by averaging the fluxes over large areas along the edges. Hence, the trends shown in Fig. 11 at the edge of the emission could well suffer from the same uncertainties. However, the trends that we detected in Fig. 11 do not depend sensitively on the spectral index computed in the shell at the edge of the emission. Although not a proof, the fact that apart from the region NW of the NW relic, the other diffuse sources do not show steep spectra at their edges, seems to suggest that despite the large uncertainties we are picking up the right trends in the NW relic too. New imaging reconstruction algorithms are being developed (e.g. Wiaux et al. 2009; Carrillo et al. 2013; Junklewitz et al. 2013) and will shed light on these issues in the next future.

7. Discussion

7.1. Dynamics of the merger

From the analysis of the optical, X-ray, and radio data we can infer some details about the cluster structure and the merger geometry. The optical analysis shows that the cluster is elongated, likely along an intergalactic filament. In the plane of the sky, it is $20'$ (6 Mpc) wide and appears to stretch from the SE to the NW. The cluster is undergoing a major merger (SEc - NWc) that is misaligned with the direction of accretion (see Fig 6). The elongated X-ray emission suggests a past merger between the SEc and NEc sub-clusters. The NW relic is located at a projected distance of $\sim$ 400 kpc from the cluster X-ray center, while the SE relic is at $\sim$ 2.8 Mpc, which is almost the virial radius for a cluster of this mass.

The different projected distances of the relics from the cluster center indicate that the shock waves are asymmetrical. We can offer two possible explanations for the origin of radio relics:
(i) a sub-group was accreting along the NW-SE direction, along the intergalactic filament, generating a first shock wave at its first passage through the cluster (SE relic) and a second shock wave (NW relic) on its second core passage (see Fig. 12 for a schematic representation of this merger scenario). In this scenario, the mass of the sub-group has to be small, otherwise the shocks would have appeared much more symmetrical about the X-ray center. The remnant of the group could be identified in the NW group. The differences in cluster-centric distances could be used to infer the time between the core passages. A Mach number of $\sim$ 3.7 corresponds to a velocity of $\sim$3700 km s^{-1} in the ICM. If the shock velocity has remained constant, we estimate that the shock took 0.7 Gyr to travel from the cluster centre to its position. Similarly, we derive a time of 0.07 Gyr for the shock responsible for the NW relic emission. If they are both caused by the same subgroup at two different core passages the time between the core passages is $\sim$0.6 Gyr. This is just a rough estimate since shock waves change their Mach number while travelling through the ICM, and the exact path they have travelled is difficult to model. To complicate matters, the small projected distance ($\sim$ 400 kpc) of the NW relic suggests that projection effects may be important.
(ii) the SE relic traces a shock caused by the infall of the SEext group into the main cluster, and the NW relic could be due to a past merger episode (e.g. to the interaction with the NW group). Such a scenario resembles the situation in the nearby Coma cluster, where a group is falling into the cluster, and a radio relic appears to be trailing it (Ogrean et al. 2012). However, the curvature and the position of the SE relic do not seem to be connected to the SEext group. Velocity information would be required to shed light on the geometry of the system and to infer the direction of accretion onto the cluster in both directions (SE and NW).

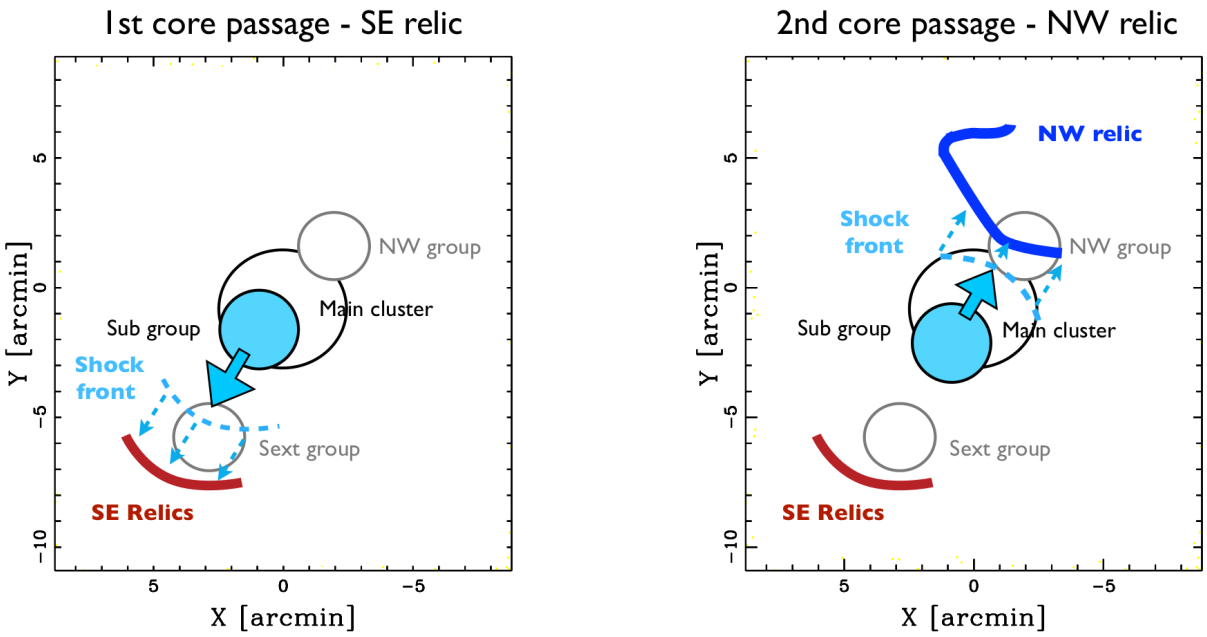

Fig. 12.— Schematic representation of a possible merger scenario (case i in Sec. 7.1). The cyan arrows indicate the direction of the motion of the sub-group, dashed lines represent the shock fronts, dashed arrows the direction of the shock fronts that will possibly create the relics. Left panel: First core passage and creation of the shock wave that generated the SE relic. Right panel: second core passage and generation of the shock front responsible for the NW relic.

7.2. Origin of the steep-spectrum emission ahead of the NW relic.

The steep spectrum emission detected NW of the NW relic is difficult to explain. According to DSA models, the shock is located where the radio spectral index is the flattest, and steeper radio emission is found downstream of the shock. Here, we detect steep emission either side of the region with the flattest spectrum. In order to explain the emission ahead of the relic, one could imagine that the particles accelerated at the shock diffuse ahead of it, producing synchrotron radiation in the upstream magnetic field (the so-called shock-precursor). The diffusion length L is $L \sim \frac{D}{v}$ with D being the diffusion coefficient and v the velocity of the particles in the upstream region. Assuming a magnetic field of 1 μGauss, for 10 GeV electrons the Bohm diffusion is $\sim 3 \times 10^{23} cm^2 s^{-1}$. For typical velocities $v \sim 10^8 cms^{-1}$, we obtain $L \sim 0.001$ pc, which is orders of magnitude smaller than the 100s kpc over which the emission is detected. Alternatively, the shock producing the NW relic could be curved in a direction perpendicular to the plane of the sky with the center of curvature lying NW of the relic. Thus, lines-of-sight that are tangents to the shock surface show the flattest spectrum. Lines-of-sight either side of it pierce regions that contain plasma that has aged and thus yield steeper spectra. This is a somewhat contrived case because it is difficult to explain why an outgoing merger shock wave should assume such a convex shape and why the spectra are steeper towards the cluster outskirts. We cannot exclude that a complex shock structure observed in projection leads to unexpected trends of the spectral index (e.g. Skillman et al. 2013).

7.3. Re-acceleration of fossil radio plasma from AGN

The complex radio emission detected around the NW relic suggests that relativistic particles are supplied by neighbouring radio-galaxies. In particular, a large radio galaxy (at a redshift of the cluster the radio galaxy would span >1.1 Mpc) is detected NE of the NW relic. Even though, no optical counterpart has been found, the radio images and spectral index maps suggest that the plasma of the Eastern lobe of the radio galaxy is spatially connected to the radio relic. The morphology and the spectral features of the NW relic, NE

filament and radio-galaxy suggest that the radio-galaxy (lobe E and lobe W) is supplying part of the electrons that are re-accelerated by a shock wave in the relic. However, the lifetime of relativistic electrons is short. At redshift of $z = 0.39$, the lifetime is limited by Inverse-Compton losses, which limits the lifetime of GeV electrons to less than 10^9 yrs[5]. Electrons with Lorentz factors $\gamma_L < 10^2$) have radiative lifetimes larger than the Hubble time. Within an assumed maximum AGN lifetime of ~ 1 Gyr and a velocity (either a diffusion or bulk velocity) of $\sim 10^8$ cm s^{-1}, these low-energy electrons cannot travel more than ~ 1 Mpc in the ICM.
In conclusion, the NE radio galaxy cannot be responsible for the electrons along the entire NW relic. We have to assume that at least a couple of other radio galaxies have injected CR electrons into the pre-shock region.
Under certain conditions, the spectral features of the radio emission will be determined by the particles injected by the shock: following Kang and Ryu (2011), we assume that the momentum spectrum of a pre-existing population of electrons ($f_{pre}(p)$) can be described by a power law with:

$$f_{\rm pre}(p) \propto p^{-s}, \quad (1)$$

and that the shock is injecting particles, above the injection momentum $p_{\rm inj}$:

$$f_{\rm inj}(p) \propto p^{-q}. \quad (2)$$

If the Mach number of the shock is ≥ 3, and $s > 4$, the particles are injected at the shock front with a power-law that is steeper than that of the pre-existing electron population (Kang and Ryu 2011, Kang et al. 2012). In this case, the particles in the downstream region will be dominated by the injected particles rather than by the pre-existing population of electrons. In the downstream region, at $p >> p_{\rm inj}$ the spectrum will be:

$$f_{\rm down}(p) \propto p^{-q}. \quad (3)$$

Hence, the spectral features of the radio emission will be set exclusively by the shock acceleration and lose all memory of the spectrum of the seed electrons. In this case, one can imagine that the electrons come from the activity of radio galaxies and diffuse into the ICM outskirts. The difference in the spectral index features of the pre-existing populations would be erased by the particles injected by the shock.
If the electrons are supplied by radio galaxies, several puzzles posed by radio relics could be solved:

- Low-Mach number shocks are not efficient in accelerating particles from the thermal pool, but are efficient enough to re-accelerate cosmic rays from past radio galaxy activity.

- Relics are not detected in every merging galaxy cluster. This suggests that a shock wave alone is not sufficient to explain the radio emission. It is also required that a pool of pre-accelerated CRs be present at the location of the relic. Along intergalactic filament the density of galaxies is higher than in other places equally distant from the cluster center. Hence, it is reasonable to assume that a larger number of electrons are injected by AGN.

- No gamma-ray emission is detected in clusters with radio relics, challenging the DSA scenario, (Vazza & Brueggen 2013). If the jet composition is leptonic (Reimer & Böttcher 2013; Yang et al. 2013; Zhang et al. 2013), no protons would be injected and hence accelerated by shock waves. Although recently Trigo et al (2013) have found evidence for a baryonic composition of the jets, the debate is still open for AGN-jets (e.g. Reimer & Böttcher 2013) .

We note that the proposed scenario is different from the one proposed by Enßlin & Gopal-Krishna (2001), where the fossil radio plasma is reenergised by adiabatic compression, and it is not yet mixed with the ICM thermal plasma.

8. Conclusions

We have presented a multi-wavelength analysis of the galaxy cluster PLCKG287.0 +32.9, that might shed new light on the origin of radio relics. Our results can be summarised as follows:

[5]For reference: we follow here Kang, Ryu and Jones (2011)

- Optical data suggests that PLCKG287.0 +32.9 is located within a 6-Mpc long intergalactic filament. The cluster has undergone a major merger (NWc -SEc), slightly misaligned with respect to the main direction of accretion. Along the filament two subclumps are detected. The galaxies along the intergalactic filament, as well as the two subclumps (SEext and NW), are likely on the process of accretion onto the main cluster.

- Two radio relics and a radio halo are present in the cluster. Additional emission is detected NW of the relic. Another relic is located SE of the cluster, at a projected distance of 2.8 Mpc. A radio halo is located in the cluster center, and filamentary emission is detected around both relics.

- The large projected distance of the SE relic and the small projected distance on the NW relic are interpreted as shock waves produces at different times during a minor merger event. A sub-cluster (with a mass ~ 0.1 of the main one) could have caused a first shock wave at his first infall onto the main cluster, and a second shock wave during the second core-passage (NW relic). The radio halo could be due to the major merger between the SEc and NEc sub-clusters.

- The NW relic emission fades into the lobes of a radio galaxy, indicating that radio relics originate from electrons previously injected by AGN and reaccelerated, likely by a shock wave. The spectral index analysis supports this interpretation. However, it is necessary to assume that two or more radio sources have injected electrons into the pre-shock region to account for the relic size.

We thank F. Vazza and T. Jones for useful discussions. A.B. and M.B acknowledge support by the research group FOR 1254 funded by the Deutsche Forschungsgemeinschaft: "Magnetisation of interstellar and intergalactic media:the prospects of low-frequency radio observations". The National Radio Astronomy Observatory is a facility of the National Science Foundation operated under cooperative agreement by Associated Universities, Inc. We thank the staff of the GMRT that made these observation possible. GMRT is run by the National center for Astrophysics of the Tata Institute of Fundamental Research. RJvW is supported by NASA through the Einstein Postdoctoral grant number PF2-130104 awarded by the Chandra X-ray Center, which is operated by the Smithsonian Astrophysical Observatory for NASA under contract NAS8-03060. This research has made use of the NASA/IPAC Extragalactic Data Base (NED) which is operated by the JPL, California Institute of Technology, under contract with the National Aeronautics and Space Administration.

REFERENCES

Bagchi, J., Durret, F., Neto, G. B. L., & Paul, S. 2006, Science, 314, 791

Bagchi, J., Sirothia, S. K., Werner, N., et al. 2011, ApJ, 736, L8

Bertin, E. & Arnouts, S. 1996, A&AS, 117, 393

Bonafede, A., Brüggen, M., van Weeren, R., et al. 2012, MNRAS, 426, 40

Bonafede, A., Giovannini, G., Feretti, L., Govoni, F., & Murgia, M. 2009, A&A, 494, 429

Brüggen, M., Bykov, A., Ryu, D., & Röttgering, H. 2011, Space Sci. Rev., 138

Buote, D. A. 2001, ApJ, 553, L15

Carrillo, R. E., McEwen, J. D., & Wiaux, Y. 2013, ArXiv e-prints

Cassano, R. & Brunetti, G. 2005, MNRAS, 357, 1313

Cassano, R., Ettori, S., Brunetti, G., et al. 2013, ApJ, 777, 141

Cassano, R., Ettori, S., Giacintucci, S., et al. 2010, ApJ, 721, L82

Condon, J. J., Cotton, W. D., Greisen, E. W., et al. 1998, AJ, 115, 1693

Cotton, W. D. 2008, PASP, 120, 439

Dolag, K., Bykov, A. M., & Diaferio, A. 2008, Space Science Reviews, 134, 311

Enßlin, T., Pfrommer, C., Miniati, F., & Subramanian, K. 2011, A&A, 527, A99

Enßlin, T. A. & Gopal-Krishna. 2001, A&A, 366, 26

Feretti, L., Giovannini, G., Govoni, F., & Murgia, M. 2012, A&AR

Ferrari, C., Govoni, F., Schindler, S., Bykov, A. M., & Rephaeli, Y. 2008, Space Science Reviews, 134, 93

Fujita, Y., Takizawa, M., & Sarazin, C. L. 2003, ApJ, 584, 190

Giacintucci, S., Dallacasa, D., Venturi, T., et al. 2011, A&A, 534, A57

Giovannini, G., Bonafede, A., Feretti, L., et al. 2009, A&A, 507, 1257

Giovannini, G., Feretti, L., Venturi, T., Kim, K.-T., & Kronberg, P. P. 1993, ApJ, 406, 399

Iapichino, L. & Brüggen, M. 2012, MNRAS, 423, 2781

Intema, H. T., van der Tol, S., Cotton, W. D., et al. 2009, A&A, 501, 1185

Intema, H. T., van Weeren, R. J., Röttgering, H. J. A., & Lal, D. V. 2011, A&A, 535, A38

Junklewitz, H., Bell, M. R., Selig, M., & Enßlin, T. A. 2013, ArXiv e-prints

Kang, H. & Ryu, D. 2011, ApJ, 734, 18

Kang, H., Ryu, D., & Jones, T. W. 2012, ApJ, 756, 97

Keshet, U. & Loeb, A. 2010, ApJ, 722, 737

Macario, G., Markevitch, M., Giacintucci, S., et al. 2011, ApJ, 728, 82

Macario, G., Venturi, T., Intema, H. T., et al. 2013, A&A, 551, A141

Nonino, M., Dickinson, M., Rosati, P., et al. 2009, ApJS, 183, 244

Ogrean, G. A., Brüggen, M., van Weeren, R. J., et al. 2013, MNRAS, 433, 812

Orrú, E., Murgia, M., Feretti, L., et al. 2007, A&A, 467, 943

Perley, R. A. & Butler, B. J. 2013, ApJS, 206, 16

Petrosian, V., Bykov, A., & Rephaeli, Y. 2008, Space Sci. Rev., 134, 191

Pinzke, A., Oh, S. P., & Pfrommer, C. 2013, MNRAS, 435, 1061

Pisani, A. 1993, MNRAS, 265, 706

Reimer, A. & Böttcher, M. 2013, Astroparticle Physics, 43, 103

Rottgering, H. J. A., Wieringa, M. H., Hunstead, R. W., & Ekers, R. D. 1997, MNRAS, 290, 577

Russell, H. R., van Weeren, R. J., Edge, A. C., et al. 2011, MNRAS, 417, L1

Scaife, A. M. M. & Heald, G. H. 2012, MNRAS, 423, L30

Skillman, S. W., O'Shea, B. W., Hallman, E. J., Burns, J. O., & Norman, M. L. 2008, ApJ, 689, 1063

Skillman, S. W., Xu, H., Hallman, E. J., et al. 2013, ApJ, 765, 21

Sommer, M. W. & Basu, K. 2013, ArXiv e-prints

van Weeren, R. J., Brüggen, M., Röttgering, H. J. A., et al. 2011, A&A, 533, A35

van Weeren, R. J., Röttgering, H. J. A., Bagchi, J., et al. 2009, A&A, 506, 1083

van Weeren, R. J., Röttgering, H. J. A., Brüggen, M., & Hoeft, M. 2010, Science, 330, 347

van Weeren, R. J., Röttgering, H. J. A., Rafferty, D. A., et al. 2012, A&A, 543, A43

Vazza, F. & Brueggen, M. 2013, ArXiv e-prints

Vazza, F., Brüggen, M., van Weeren, R., et al. 2012, MNRAS, 421, 1868

Vazza, F., Brunetti, G., & Gheller, C. 2009, MNRAS, 395, 1333

Vazza, F., Dolag, K., Ryu, D., et al. 2011, MNRAS, 418, 960

Venturi, T., Giacintucci, S., Brunetti, G., et al. 2007, A&A, 463, 937

Wiaux, Y., Jacques, L., Puy, G., Scaife, A. M. M., & Vandergheynst, P. 2009, MNRAS, 395, 1733

Yang, H.-Y. K., Ruszkowski, M., & Zweibel, E. 2013, MNRAS

Zhang, J., Sun, X.-N., Liang, E.-W., et al. 2013, ArXiv e-prints

This 2-column preprint was prepared with the AAS LaTeX macros v5.2.